Using Spherical Harmonics to Model Mutual Coupling Effects on Embedded Element Patterns

Tworit Dash*, Nehir Berk Onat*, Yanki Aslan*, and Alexander Yarovoy*
* Microelectronics, Delft University of Technology, Netherlands
{t.k.dash, n.b.onat, y.aslan, a.yarovoy}@tudelft.nl

2025 International Conference on Electromagnetics in Advanced Applications (ICEAA) | 979-8-3315-4472-0/25/$31.00 ©2025 IEEE | DOI: 10.1109/ICEAA65662.2025.11305766

***Abstract*—The reconstruction of *Embedded Element Patterns* (EEP) in an array of antennas is presented as an attempt to understand the effects of *Mutual Coupling* (MC) among the antenna elements. The EEP far fields are modeled with a weighted sum of orthonormal spherical harmonic basis functions (explained by their mode numbers). The weight of each significantly contributing mode is estimated by the *Singular Value Decomposition* (SVD) approach. A practical example of a non-uniform array of circular patch antennas is considered for analyzing the significant contributing modes. Although the values of the weights of the modes are different for each antenna element in the array, the contributing modes remain very similar for all the elements, indicating that the mutual coupling can be sufficiently explained by a limited number of variables (weights) corresponding to limited spherical harmonic modes. The reconstructed patterns are validated by comparing them with full-wave simulation results.**

***Index Terms*—Mutual coupling, embedded element pattern, spherical harmonics.**

I. Introduction

ALMOST all modern applications involving radar or communication technologies (automotive [1], [2]; biomedical [3]; meteorology [4], [5], and so on) employ antenna arrays for the transmission and reception of electromagnetic waves. Antenna arrays are used to steer a directive beam toward the direction of interest. Furthermore, irregular *Multiple-Input Multiple-Output* (MIMO) antenna arrays have been proposed for high-resolution imaging, such as airborne radars [6], automotive radars [7] and (near-field) radar imaging [8], [9].

The optimal positioning of the antennas in an array is decided based on the application of interest and on several output parameters, such as the cross-polar and *Side Lobe Levels* (SLL) or aperture efficiency. These optimization problems are usually addressed by assuming that the radiation pattern of each antenna element in the array (or the EEP) is identical. In other words, the existing algorithms ignore the effect of MC between the antenna elements, and the resulting asymmetries in the embedded element patterns (EEPs) are usually discarded [10], [11], [12], [13]. This leads to significant deviations from the predicted goals, such as SLLs [14], and the sensing performance degrades in real-life operation [15]. Furthermore, the accurate knowledge of EEPs across the whole frequency band and field-of-view becomes critical for calibration [16].

To understand MC, we have analyzed the EEP far-fields in this paper. Although they are excited at a specific frequency corresponding to the fundamental mode of the circular patch, due to the MC, the far field pattern of each element is very sensitive to the position of the element in the array and the positions of the other elements with respect to it. The EEP far-fields no longer remain symmetric in either the E- or H-plane. In addition to that, sometimes, irrespective of the array type (even for a single antenna without an array), size, or spacing, the EEP far-fields can have degraded patterns due to environmental factors, such as the temperature of the circuitry movement of the platform on which it is mounted, and so on.

Because each EEP field is very different from the others and sensitive to the above-mentioned factors, it is usually a challenging task to generalize these patterns. Generalizing means that one should find a suitable function with a few parameters that can sufficiently explain these patterns quantitatively. A rigorous approach would be to model the currents on the patches based on their locations, the locations of the nearby elements, and the effects of extra EM waves like the surface waves. However, it is usually a very cumbersome task because fitting the near-field currents would require us to model the currents with a lot of variables. On the other hand, as the far-fields are functions of the integrated near-fields, they are forgiving to local current distributions. Therefore, so many variables/ effects would be unnecessary to explain the EEP far-field patterns sufficiently.

This paper presents a methodology to characterize the effect of mutual coupling on the EEP far-fields with a relatively low number of parameters. This helps us effectively model the EEP far-fields for any antenna system. In this paper, we have chosen the spherical harmonic basis functions to generalize these far-field patterns. These basis functions are characterized by mode numbers $l \in \mathbb{Z}^+$ and $m \in \mathbb{Z}^+$, and each specific combination of these mode numbers gives rise to a distinct far-field pattern. The complex EEP far-fields are assumed to be explained by a weighted sum of these modes. The asymmetry in the patterns could be explained by estimating the weights of each mode. After knowing the dominant modes that can explain the EEP far-fields of the majority of the antenna elements in an array (by performing randomized tests), the weights can be reused for other purposes, such as predicting the patterns for another (unknown) configuration of the array [17], [18]. This way of representing the complex patterns is much more efficient and requires much less time than the full-wave simulations. This paper, however, does not focus on the use cases of the estimated weights but focuses more on the estimation of these weights and the reconstruction of the EEP far-fields. The pattern stability against small errors in the weights is also studied, providing valuable inputs for the potential use cases.

Although the proposed procedure is generic and applicable to various scenarios, in this paper, we have validated our results against full-wave simulations of an array of pin-fed circular patch antennas.

The main body of the paper is organized as follows. The spherical harmonics and the model of the EEP are discussed in Section II. Section III explains the EEP far-field reconstruction using the estimated spherical harmonic coefficients. Section IV presents the *Antenna Under Test* (AUT). Section V shows an approach to finding the significant number of spherical harmonic mods. The results are presented in Section VI, and Section VII concludes the paper.

II. Spherical Harmonics

The EEP far-field patterns are decomposed into modes of spherical harmonics. The complex electric field can be represented as a weighted sum [19, Eq. (2.2)]:

$$E(\theta,\phi) = \sum_{l=0}^{\infty} \sum_{m=-l}^{+l} c_l^m Y_l^m(\theta,\phi), \tag{1}$$

where

$$Y_l^m(\theta,\phi) = \sqrt{\frac{2l+1}{4\pi}\frac{(l-|m|)!}{(l+|m|)!}} P_l^{|m|}(\cos\theta)\exp(\mathrm{j}m\phi), \tag{2}$$
$$l \in [0,\infty], m \in [-l,+l],$$

where the numbers l, and m represent the mode indices, θ is the elevation angle, ϕ is the azimuth angle in standard spherical coordinate system, P_l^m are the associated Legendre functions of lth degree (or level) and mth order (modes). The c_l^m in (1) are the complex weights of these modes. These modes are orthonormal, meaning that:

$$\int_{\Omega} Y_l^m(\theta,\phi) Y_{l'}^{m'}(\theta,\phi) d\Omega = \delta_{ll'}\delta_{mm'} \tag{3}$$

where δ is the Dirac delta function and Ω is the surface area. In matrix form, (1) can be written as:

$$\mathbf{e} = \mathbf{Y}\mathbf{c}, \tag{4}$$

where $\mathbf{Y} \in \mathbb{C}^{(N_\theta N_\phi)\times L^2}$ has all the spherical wave mode basis functions $\mathbf{Y} = [\mathbf{y}_0^0, \mathbf{y}_1^{-1}, \mathbf{y}_1^0, \mathbf{y}_1^1, \cdots, \mathbf{y}_{L-1}^{L-1}]$ ($L-1$ being the highest degree, L being the number of degrees used). Entries to this matrix $\mathbf{Y}$, i.e., $\mathbf{y}_l^m \in \mathbb{C}^{(N_\theta N_\phi)\times 1}$ are vectorized form of the spherical modes, where N_θ and N_ϕ are the number of elevation and azimuth directions, respectively. Therefore, $\mathbf{c} \in \mathbb{C}^{L^2\times 1}$, where $\mathbf{c} = [c_0^0, c_1^{-1}, c_1^0, c_1^1, \ldots, c_{L-1}^{L-1}]^{\mathrm{T}}$. Uppercase and lowercase bold fonts refer to matrices and vectors, respectively. Therefore, the vector $\mathbf{e} \in \mathbb{C}^{(N_\theta N_\phi)\times 1}$.

III. EEP Far Field Reconstruction

Given a noisy vectorized far-field measurement, $\mathbf{f} \in \mathbb{C}^{(N_\theta N_\phi)\times 1}$, the coefficients $\mathbf{c}$ are estimated using least squares:

$$\hat{\mathbf{c}} = \left(\mathbf{Y}^{\mathrm{H}}\mathbf{Y}\right)^{-1}\mathbf{Y}^{\mathrm{H}}\mathbf{f}, \tag{5}$$

where $\mathbf{Y}^\dagger = (\mathbf{Y}^{\mathrm{H}}\mathbf{Y})^{-1}\mathbf{Y}^{\mathrm{H}}$ is the Moore-Penrose inverse [20]. We employ a *Singular Value Decomposition* (SVD)-based approach for computational efficiency and numerical stability via low-rank approximation. The basis function matrix $\mathbf{Y}$ (with independent columns) is decomposed as [20]:

$$\mathbf{Y} = \mathbf{U}\mathbf{\Sigma}\mathbf{V}^{\mathrm{H}}, \tag{6}$$

where $\mathbf{U} \in \mathbb{C}^{N_\theta N_\phi \times N_\theta N_\phi}$ is a complex unitary matrix, $\mathbf{\Sigma} \in \mathbb{C}^{N_\theta N_\phi \times L^2}$ is a rectangular diagonal decaying matrix with non-negative real numbers on the diagonal, and $\mathbf{V} \in \mathbb{C}^{L^2\times L^2}$ is a complex unitary matrix. The coefficients are then computed as:

$$\hat{\mathbf{c}} = \mathbf{V}\mathbf{\Sigma}^{-1}\mathbf{U}^{\mathrm{H}}\mathbf{f}. \tag{7}$$

After the coefficients are computed, the reconstruction of the absolute electric field can be determined using:

$$\hat{\mathbf{e}} = \mathbf{Y}\hat{\mathbf{c}}. \tag{8}$$

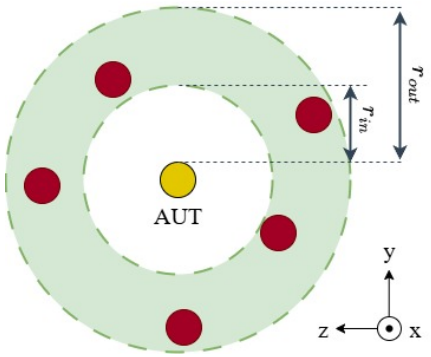

Fig. 1. K = 6-element aperiodic array topology (each embedded element having five neighboring elements) where the AUT, highlighted with the yellow color, is located at the center, $(y_o, z_o) = (0,0)$, and the neighboring elements (red colored) are randomly positioned in the defined green region: $r_{in}^2 \leq (y_i^2 + z_i^2) \leq r_{out}^2$ where (y_i, z_i) is the location of the i-th neighbor element in λ.

IV. Antenna Under Test (AUT)

This study investigates a K-element, irregularly spaced, pin-fed circular patch antenna array operating at a center frequency of 10 GHz. An example of the array topology is depicted in Fig. 1, with key design parameters listed in Table I. The objective is to estimate the EEP of the AUT, which is located at the origin $(0,0)$. The remaining elements are randomly distributed within a defined area bounded by an inner and outer circle. The inner circle has a radius of $r_{in} = 0.5\lambda$, where λ represents the wavelength, and the outer circle has a radius of $r_{out} = \lambda$, enabling the analysis of MC effects on the EEPs through close element spacing. A minimum inter-element distance of 0.5λ is enforced to ensure a quasi-random layout.

TABLE I
Antenna Design Parameters

Center frequency	10 GHz	**Aperture length** ($\mathrm{A_y}$)	2λ
Patch radius	4.44 mm	**Aperture width** ($\mathrm{A_z}$)	2λ
Feeding type	pin-fed	**Substrate height** (h)	0.41 mm
Circle rad. [r_1,r_2]	$[0.5,1]\lambda$	**Relative permittivity** (ϵ_r)	3.55

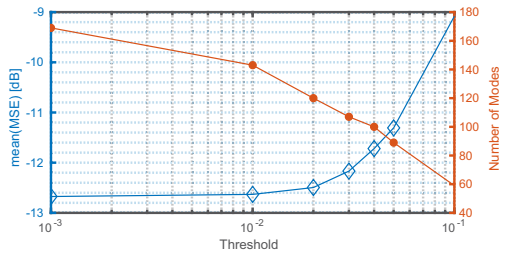

Fig. 2. An example comparison plot showing the selected number of modes with a defined threshold for the absolute value of the coefficients, where MSE quantifies the error over the six-element topology dataset comprising 3431 randomly generated topology.

V. Finding Significant Spherical Modes

Following the AUT topology in Fig. 1 and the discussion in Section III, the number of significant modes is determined as $L^2 = 169$ (after a manual investigation), though further reduction is possible by eliminating modes with near-zero values without compromising the field reconstruction performance. The optimal number of modes is selected based on dataset analysis to balance accuracy and efficiency. The reconstruction error is quantified using the *Mean Square Error* (MSE) in the decibel scale:

$$\mathrm{MSE}^{(\mathrm{dB})} = 10\log\left(\frac{1}{N_\theta N_\phi}\left(\mathbf{e}-\hat{\mathbf{e}}\right)^{\mathrm{H}}\left(\mathbf{e}-\hat{\mathbf{e}}\right)\right), \qquad (9)$$

where the vector $\mathbf{e}$ comprises the full-wave simulated electric field of the chosen element in the far-field region that is generated by the commercial full-wave simulator CST, and $\hat{\mathbf{e}}$ is the corresponding reconstructed pattern in vector form as given in (8), but with truncated versions of $\mathbf{Y}$ and $\hat{\mathbf{c}}$.

The relation between the MSE, the chosen absolute threshold value for the coefficients, and the number of modes was investigated in each dataset to find the optimal number of modes. As each topology comprising a different number of elements shows a similar behavior, Fig. 2 illustrates this relation for the five neighboring-element dataset (total six elements) comprising 3431 (an arbitrarily large number) randomly generated topologies. The mean MSE and the number of modes are related inversely. With an increase in the threshold, the mean MSE increases while the number of modes decreases (represented by the two lines in Fig. 2). A compromise can be taken as the intersection of these two lines, which occurs at around 95 modes.

VI. Results

The reconstruction results of the amplitude and the phase of the complex EEP far-field of one element in the array configuration with five neighboring elements are shown in Fig. 3. The number of modes used to reconstruct these patterns is 95. If we compare the reconstructions in Fig. 3a, and Fig. 3d with full-wave ones in Fig. 3c, and Fig. 3f, respectively, it can be observed that the reconstruction is adequate for both the amplitude and the phase. To verify robustness of the reconstruction, a complex-valued white Gaussian noise with a noise standard deviation of 1% of the coefficient values has been added to the estimated weights of the modes $\hat{\mathbf{c}}$:

$$\hat{\mathbf{c}}^{(\mathrm{err})} = \hat{\mathbf{c}} + \mathbf{n}, \text{ where } \mathbf{n} \overset{i.i.d}{\sim} \mathcal{CN}(\mathbf{0}, \mathrm{diag}\left(\hat{\mathbf{c}}^2/10^4\right)). \qquad (10)$$

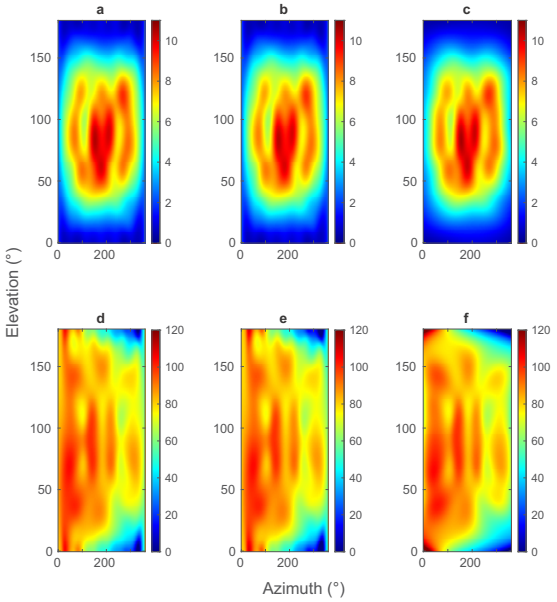

Fig. 3. Example reconstruction of the EEP of one element in the array: (a) and (d) illustrate the amplitude and phase reconstruction with spherical harmonics complex weights $\hat{\mathbf{c}}$, respectively; (b) and (e) display the amplitude and phase reconstruction with (1% standard deviation) added complex Gaussian random noise on top of the complex weights, i.e., $\hat{\mathbf{c}}^{(\mathrm{err})}$, (c) and (f) show the amplitude and phase of the full-wave simulation, respectively. The amplitudes are the electric (E-)field magnitude in linear scale (for the reference of 1W peak power and 1 meter distance), and the corresponding phases are in degrees (°).

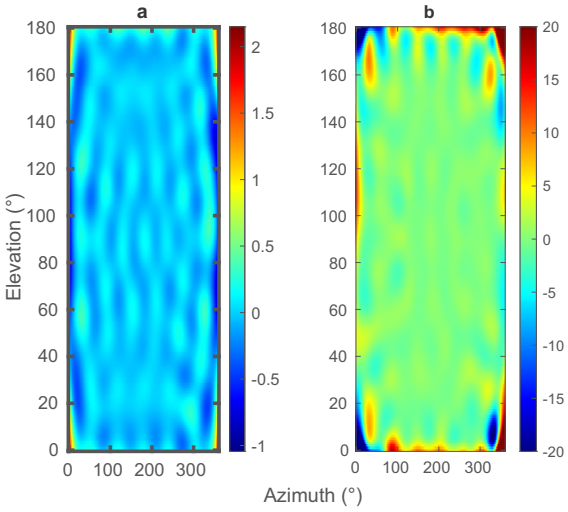

Fig. 4. Difference between the reconstructed E-field pattern and the full-wave simulation results (for the reference of 1W peak power and 1 meter distance): (a) magnitude difference $|\hat{\mathbf{e}}| - |\mathbf{e}|$ in linear; (b) phase difference $\angle\hat{\mathbf{e}} - \angle\mathbf{e}$ in degrees (°).

The reconstruction results (Fig. 3b and 3e) indicate that the reconstruction is robust to errors induced in the coefficients. The difference between the reconstructed and the full-wave patterns are shown in Fig. 4 for both the amplitude ($|\hat{\mathbf{e}}| - |\mathbf{e}|$) and the phase ($\angle\hat{\mathbf{e}} - \angle\mathbf{e}$). Noticeable differences between the reconstructions and the full-wave patterns can be especially observed at the edges of the field of view. The same procedure can be followed but with more spherical wave modes at the

cost of reduced computational efficiency if finer reconstruction is required.

VII. Conclusions

A novel methodology to efficiently model the MC effects on the complex-valued EEP far-fields is presented. A more generic decomposition of the EEP far-fields is proposed with spherical harmonics. The decomposition is carried out with SVD algorithm, which makes it numerically stable and computationally efficient. A suitable number of significantly contributing modes can, therefore, be decided by thresholding based on the requirements of the application of interest. An example of the number of contributing modes is presented by considering the MSE for the estimated patterns. It is shown that the reconstruction is adequate for both the amplitude and the phase of the EEP far-fields except for the edges of the field of view. The results of this study suggest that the proposed methodology can efficiently be applied to antenna array problems for calibration or optimization purposes. Future work will consider a potential method where the spherical wave coefficients can be predicted and subsequently used to reconstruct the EEP of an AUT for a given aperiodic topology.

References

[1] S. Yuan, F. Fioranelli, and A. G. Yarovoy, "Vehicular-motion-based doa estimation with a limited amount of snapshots for automotive mimo radar," *IEEE Transactions on Aerospace and Electronic Systems*, vol. 59, no. 6, pp. 7611–7625, 2023.

[2] I. Roldan, F. Fioranelli, and A. Yarovoy, "Self-supervised learning for enhancing angular resolution in automotive mimo radars," *IEEE Transactions on Vehicular Technology*, vol. 72, no. 9, pp. 11 505–11 514, 2023.

[3] C. Li, V. M. Lubecke, O. Boric-Lubecke, and J. Lin, "A review on recent advances in doppler radar sensors for noncontact healthcare monitoring," *IEEE Transactions on Microwave Theory and Techniques*, vol. 61, no. 5, pp. 2046–2060, 2013.

[4] R. Palmer, D. Bodine, P. Kollias, D. Schvartzman, D. Zrnić, P. Kirstetter, G. Zhang, T.-Y. Yu, M. Kumjian, B. Cheong, S. Collis, S. Frasier, C. Fulton, K. Hondl, J. Kurdzo, T. Ushio, A. Rowe, J. Salazar-Cerreno, S. Torres, M. Weber, and M. Yeary, "A primer on phased array radar technology for the atmospheric sciences," *Bulletin of the American Meteorological Society*, vol. 103, no. 10, pp. E2391 – E2416, 2022. [Online]. Available: https://journals.ametsoc.org/view/journals/bams/103/10/BAMS-D-21-0172.1.xml

[5] T. Dash, A. Gîrdianu, O. A. Krasnov, and A. G. Yarovoy, "Beamforming for a Fast Scanning Phased Array Weather Radar," in *Proceedings of the 20th European Radar Conference*, 2023, pp. 290–293.

[6] E. Loew and R. L. Haupt, "Two-way pattern synthesis for the airborne phased array radar (apar)," in *2022 IEEE International Symposium on Phased Array Systems Technology (PAST)*, 2022, pp. 1–3.

[7] S. Sun and Y. D. Zhang, "4d automotive radar sensing for autonomous vehicles: A sparsity-oriented approach," *IEEE Journal of Selected Topics in Signal Processing*, vol. 15, no. 4, pp. 879–891, 2021.

[8] X. Zhuge and A. G. Yarovoy, "Study on two-dimensional sparse mimo uwb arrays for high resolution near-field imaging," *IEEE Transactions on Antennas and Propagation*, vol. 60, no. 9, pp. 4173–4182, 2012.

[9] X. Zhuge, A. G. Yarovoy, T. Savelyev, and L. Ligthart, "Modified kirchhoff migration for uwb mimo array-based radar imaging," *IEEE Transactions on Geoscience and Remote Sensing*, vol. 48, no. 6, pp. 2692–2703, 2010.

[10] J. Wang, P. Aubry, and A. Yarovoy, "3-d short-range imaging with irregular mimo arrays using nufft-based range migration algorithm," *IEEE Transactions on Geoscience and Remote Sensing*, vol. 58, no. 7, pp. 4730–4742, 2020.

[11] Y. Jiang, J. Dong, F. Liu, Y. Yue, and R. Shi, "Pattern synthesis of mimo radar using differential particle swarm optimization algorithm," *Optik*, vol. 126, no. 24, pp. 5781–5786, 2015.

[12] J. Wang, X. Wu, J. Ye, J. Sun, and G. Hua, "A novel two-way pattern synthesis method with the uniform and thinned arrays," *IEEE Antennas and Wireless Propagation Letters*, vol. 23, no. 10, pp. 3108–3112, 2024.

[13] R. Z. Syeda, M. C. van Beurden, and A. B. Smolders, "Sparse virtual array synthesis for mimo radar imaging systems," *IET Microwaves, Antennas & Propagation*, vol. 15, no. 11, pp. 1458–1472, 2021.

[14] W. P. Keizer, "Planar phased-array antennas: Mutual coupling and ultralow peak sidelobes," *IEEE Antennas and Propagation Magazine*, vol. 61, no. 1, pp. 14–28, 2018.

[15] E. BouDaher, F. Ahmad, M. G. Amin, and A. Hoorfar, "Effect of mutual coupling on direction-of-arrival estimation using sparse dipole arrays," in *2016 IEEE International Symposium on Antennas and Propagation (APSURSI)*, 2016, pp. 2189–2190.

[16] G. Kyriakou, M. Kovaleva, K. F. Warnick, D. B. Davidson, and P. Bolli, "Deriving mutual impedance matrix of a large antenna array from embedded element patterns with measurement noise," *IEEE Transactions on Antennas and Propagation*, vol. 73, no. 1, pp. 216–224, 2025.

[17] N. B. Onat, I. Roldan, F. Fioranelli, A. Yarovoy, and Y. Aslan, "Efficient embedded element pattern prediction via machine learning: A case study with planar non-uniform sub-arrays," in *Proc. 17th EuCAP*, 2023, pp. 1–5.

[18] N. B. Onat, I. Roldan, F. Fioranelli, A. Yarovoy, and Y. Aslan, "Constrained infinitesimal dipole modeling-assisted ensemble prediction of embedded element patterns via machine learning," *IEEE Transactions on Antennas and Propagation*, vol. 72, no. 9, pp. 7353–7358, 2024.

[19] M. Costa, A. Richter, and V. Koivunen, "Unified array manifold decomposition based on spherical harmonics and 2-D Fourier basis," *IEEE Transactions on Signal Processing*, vol. 58, no. 9, pp. 4634–4645, 2010.

[20] R. Penrose, "A generalized inverse for matrices," *Mathematical Proceedings of the Cambridge Philosophical Society*, vol. 51, no. 3, pp. 406–413, 1955.